Integrated Spatial and Single-Nuclei Transcriptomic Analysis of Long Non-Coding RNAs in Alzheimer's Disease

Bernard Ng[1,#], Denis R. Avey[1,5,#], Faraz Sultan[1], Katia de Paiva Lopes[1], Masashi Fujita[2], Devin Saunders[1], Ricardo A. Vialle[1], Himanshu Vyas[1], Nicola A. Kearns[1,5], Shinya Tasaki[1], Artemis Iatrou[1,3], Sashini De Tissera[1], Amiko Krisa Lagrimas[1], Tien-Hao Chang[1], Jishu Xu[1], Chunjiang Yu[1], Vilas Menon[2], Chris Gaiteri[1,4], Philip L. De Jager[2], David A. Bennett[1,5], Yanling Wang[1,5,*]

1. Rush Alzheimer's Disease Center, Rush University Medical Center, Chicago, IL, 60612, USA
2. Center for Translational and Computational Neuroimmunology, Department of Neurology, Columbia University Irving Medical Center, New York, NY, USA
3. Current affiliation: Department of Psychiatry, McLean Hospital, Harvard Medical School, Belmont, MA, 02478, USA
4. Department of Psychiatry, Upstate Medical University, Syracuse, NY, 13210, USA
5. Department of Neurological Sciences, Rush University Medical Center, Chicago, IL, 60612, USA

[#]Contributed equally

*Correspondence to yanling_wang@rush.edu

Abstract

Background

Long non-coding RNAs (lncRNAs) are critical regulators of physiological and pathological processes, with their dysregulation increasingly implicated in aging and Alzheimer's disease (AD). To investigate the spatial and cellular distribution of lncRNAs in the aging brain, we leveraged published spatial transcriptomics (ST), single-nucleus RNA sequencing (snRNA-seq), and bulk RNA-seq datasets from the dorsolateral prefrontal cortex (DLPFC) of ROSMAP participants with and without pathological AD.

Results

LncRNAs exhibited greater subregion-specific expression than mRNAs, with enrichment in antisense and lincRNA biotypes. Subregion-enriched lncRNAs were generally not cell-type specific, and vice versa. Differential expression analysis of ST data identified AD-associated lncRNAs with distinct spatial patterns and moderate overlap with differentially expressed (DE) lncRNAs from bulk RNA-seq. Gene set enrichment revealed their involvement in chromatin remodeling, epigenetic regulation, and RNA metabolism. We also identified AD DE lncRNAs across major brain cell types using snRNA-seq but overlap with ST DE lncRNAs was limited. Among previously reported lncRNAs, *OIP5-AS1* was consistently upregulated in AD in all cortical subregions. Antisense oligonucleotide (ASO) knockdown of *OIP5-AS1* in iPSC-derived microglia led to upregulation of pro-inflammatory genes and downregulation of DNA replication and repair pathways. Immunoassays confirmed increased secretion of pro-inflammatory cytokines. The knockdown expression pattern was enriched for microglia-specific AD DE genes and microglia states**.**

Conclusions

This study provides a spatial and cellular map of lncRNAs in the aging human cortex and identifies subregion- and cell-type-enriched DE lncRNAs in AD. Our findings implicate *OIP5-AS1* in microglial activation, suggesting its potential contribution to AD pathogenesis.

Keywords

long non-coding RNA; spatial transcriptomics; snRNA-seq; Alzheimer's disease; OIP5-AS1; microglia

Introduction

One of the most remarkable discoveries of the 21st century is that a large portion of the genome is transcribed into RNAs with little or no protein-coding potential (1,2). While approximately 90% of the human genome is transcribed, only about 2% is annotated as protein-coding genes. This paradigm-shifting discovery has spurred extensive research into the regulatory roles of non-coding RNAs in gene expression (2,3), redefining our understanding of the genome and challenging the traditional view that only protein-coding genes are functionally relevant.

Among non-coding RNAs, long non-coding RNAs (lncRNAs) represent a prominent class of transcripts longer than 200 nucleotides, predominantly transcribed by RNA Polymerase II. LncRNAs regulate gene expression through diverse mechanisms, including epigenetic modification, chromatin remodeling, and post-transcriptional processes (4,5). Compared to coding RNAs, lncRNAs exhibit greater tissue and cell-type specificity (6,7) and are particularly abundant in the human brain, where they play critical roles in neuronal differentiation, synaptogenesis, and neuroplasticity (1,8). Dysregulated lncRNA expression has been implicated in numerous neurological disorders, including Alzheimer's disease (AD). In AD, aberrant lncRNA expression has been linked to key pathological processes, such as amyloid-beta metabolism, tau pathology, neuroinflammation, and neuronal death (9–13). However, the spatial and cellular contexts in which lncRNAs might influence AD-related processes remain largely unexplored.

66 In this study, we leveraged our published spatial transcriptomics (ST) data (14) as well as published
67 single-nucleus RNA sequencing (snRNA-seq) (15) and bulk RNA-seq (16) datasets from the
68 dorsolateral prefrontal cortex (DLPFC) of ROSMAP participants to investigate the spatial and cellular
69 expression of lncRNAs in the aging brain. We identified subregion-specific lncRNAs and assessed their
70 overlap with cell-type-specific lncRNAs. Additionally, we mapped lncRNAs and mRNAs that are
71 differentially expressed (DE) in AD across distinct subregions and compared the ST findings with results
72 from bulk RNA-seq and snRNA-seq analyses. Finally, we functionally tested an AD-associated lncRNA,
73 *OIP5-AS1*, in iPSC-derived microglia using antisense oligonucleotide knockdown and revealed its
74 potential roles in AD pathogenesis.

75 **Results**

76 **Spatial expression of lncRNAs in aged human brains**

77 Using our recently published ST data (14), we analyzed lncRNA expression from 78 DLPFC sections
78 of 21 female individuals (AD = 13; no cognitive impairment (NCI) = 8). In total, we detected 7,634
79 lncRNAs and 16,769 protein-coding mRNAs across 8 spatial spot clusters corresponding to subregions:
80 layer 1 (L1), layers 2–3 (L2–3), layers 3–5 (L3–5), layer 5 (L5), layer 6 (L6), white matter (WM),
81 meninges, and blood vessels (Fig. 1A). Consistent with prior studies (6,7), lncRNAs exhibited lower
82 expression levels than mRNAs (Fig. 1B-C). For downstream analysis, we retained 1,578 lncRNAs and
83 13,808 mRNAs with adequate expression (counts per million [CPM] >1 in >80% of brain sections).
84 Among these lncRNAs, the most prevalent biotypes were long intergenic non-coding RNAs (lincRNAs)
85 and antisense transcripts (Fig. 1D). Notably, lncRNAs demonstrated greater subregion specificity, with
86 only 39.9% of lncRNAs detected across all eight subregions, compared to 89.3% of mRNAs (Fig. 1E).

87 As a data quality check, we investigated the molecular systems within each subregion by generating
88 a pseudo-bulk matrix for each subregion and performing co-expression network analysis using the

89 Speakeasy algorithm(17) (Fig. S1). This analysis generated 193 modules, each containing at least 30
90 genes (Table S2). Module preservation analysis revealed that cortical layer modules were more
91 preserved than those derived from WM, blood vessels, and meninges (Fig. S1B; Table S3). Within
92 each subregion, 15–60% of the modules were lncRNA-enriched (Fig. S1) with many enriched for
93 oxidative phosphorylation, synaptic signaling, immune response, cell cycle regulation, and ncRNA
94 processing (Table S4), in line with the functional roles of ncRNA.

95 **Comparison of subregion- and cell-type-specific lncRNA expression**

96 By contrasting the expression of spatial spots in one subregion against all others in our ST data, we
97 identified 79 subregion-specific lncRNAs (Table S1). To investigate whether subregion-specific
98 lncRNAs also exhibit cell-type specificity, we cross-referenced a published snRNA-seq dataset (15)
99 derived from the DLPFC of 424 ROSMAP participants(15). We observed limited overlap between
100 subregion-specific and cell-type-specific lncRNAs (Fig. 2A; Table S1), but some exceptions emerged.
101 For example, *AL031056.1* was enriched in L1 and astrocytes (Fig. 2C), *LINC00507* in L2–3 and
102 excitatory neurons (Fig. 2B-C), *AC021613.1* in L6 and excitatory neurons (Fig. 2B-C), and *AC092958.1*,
103 *TYMSOS*, and *LINC00844* in WM and oligodendrocytes (Fig. 2B-C). However, most subregion-specific
104 lncRNAs were expressed in all major cell types (Fig. 2C).

105 We next examined whether cell-type-specific lncRNAs exhibited subregion specificity. Although general
106 trends emerged, such as astrocyte-specific lncRNAs being more abundant in L1, excitatory/inhibitory
107 neuron-specific lncRNAs in cortical layers, and oligodendrocyte-specific lncRNAs in WM, many cell-
108 type-specific lncRNAs were expressed across multiple subregions (Fig. 2D; Table S1).

109 **AD DE lncRNAs revealed by ST**

110 To identify AD DE lncRNAs in our ST data, we aggregated spot-level expression values within each
111 brain section to generate a pseudo-bulk matrix for each subregion. We then normalized these estimates
112 using TMM-voom (18), and applied linear mixed models (LMM) to contrast AD against NCI. We
113 accounted for age, RNA Integrity Number (RIN), postmortem interval (PMI), and batch as fixed effects,
114 and within-subject correlation as a random effect. We declared differentially expressed genes at an α
115 of 0.05 with false discovery rate (FDR) correction across genes and subregions.

116 We identified 275 AD DE lncRNAs (Table S5). A greater proportion of these lncRNAs exhibited negative
117 associations with AD compared to mRNAs (Fig. 3A-B) and biotype analysis revealed enrichment of
118 bidirectional promoter lncRNAs in L3–5 and lincRNAs in L6 and WM (Fig. 3C). Next, we compared our
119 ST-derived AD DE lncRNAs with those identified from bulk RNA-seq data of the DLPFC in 1,049
120 individuals (16) (Table S5). Although the overlap of AD DE genes between ST and bulk RNA-seq was
121 modest (Fig. 3D), the set of t-values across their common lncRNAs exhibited moderate correlations
122 between the two modalities (R = 0.3; Fig. 3D). Concordant findings included several downregulated
123 lncRNAs, such as *LY86-AS1*, *FAM106A*, *LINC01007*, and *MIR7-3HG*, as well as upregulated lncRNAs,
124 including *NEAT1*, *LINC00632*, *FGD5-AS1*, and *LINC01094* (Fig. 3D).

125 To determine the potential functional roles of these AD DE lncRNAs, we applied gene set enrichment
126 analysis (GSEA) to the set of t-values across all genes for each subregion. Focusing on gene sets
127 comprising AD DE lncRNAs, we observed enrichment for processes, such as cell motility (*MALAT1*,
128 *SPATA13*), apoptosis (*ARMCX5-GPRASP2*), chromatin organization (*XIST*, *KCNQ1OT1*), and
129 regulation of defense responses (*NEAT1*) (Fig. 3E; Table S6-7). Notably, we observed enrichment for
130 HDAC targets, which included three AD DE lncRNAs, namely *FGD5-AS1*, *NNT-AS1*, and *OIP5-AS1*
131 (Fig. 3E; Table S7).

132 **AD DE lncRNAs revealed by snRNA-seq**

133 We further examined AD DE lncRNAs using the snRNA-seq data (15) and observed that more DE
134 lncRNAs are negatively associated with AD than DE mRNAs (Fig. 4A-B; Table S5), consistent with our
135 ST findings. Additionally, AD DE lncRNAs were enriched for lincRNAs, particularly in inhibitory neurons
136 and oligodendrocyte precursor cells (OPCs) (Fig. 4C). Compared to DE mRNAs, DE lncRNAs
137 displayed greater cell-type specificity in oligodendrocytes, inhibitory neurons, and excitatory neurons
138 (Fig. 4D). Overlaps between subregion-specific and cell-type-specific AD DE lncRNAs were minimal
139 (Fig. 4E). Pairwise t-value correlations revealed moderate alignment between L3–5 and inhibitory
140 neurons as well as between blood vessels and microglia/OPCs (Fig. 4F). While a larger proportion of
141 DE mRNAs were shared across subregions and cell types (Fig. 4E), t-value correlations between
142 subregions and cell types remained weak (Fig. 4G), likely reflecting technological differences between
143 ST and snRNA-seq.

144 **Subregion-resolved AD DE lncRNAs and their cell-type expression pattern**

145 We then examined the subregion specificity of AD DE lncRNAs in our ST data and found DE lncRNAs
146 to be generally more subregion-specific than DE mRNAs, with 115 of 275 DE lncRNAs showing
147 subregion-specific differential expression in the cortex (Fig. 5A; Table S5). These subregion-specific
148 DE lncRNAs, regardless of whether they were up- or downregulated, did not appear to be cell-type-
149 specific (Fig. 5B). The remaining 160 of 275 AD DE lncRNAs were differentially expressed across
150 multiple subregions, with the majority (~93%) not previously reported (Fig. 5C).

151 Some AD DE lncRNAs displayed high expression in one subregion but showed predominant AD effects
152 in other subregions. For example, *LINC00844* was highly expressed in WM/oligodendrocytes (Fig. 2B-
153 C) but exhibited its strongest AD effects in L2-3 (Fig. 5B). Similarly, *LINC00507* showed high expression
154 in L2-3 but demonstrated predominant AD effects in L3-6 (Fig. 5C).

155 Among previously reported AD DE lncRNAs (9–12,19) (Figure 5C), we observed higher expression of
156 *MALAT1*, *NEAT1, and XIST* in subregion(s) of AD individuals, Interestingly, *MALAT1 has been* reported
157 to suppresses neuronal apoptosis and inflammation and promote neurite outgrowth in AD cellular
158 models(20,21). *NEAT1* induces Aβ-induced neuronal damage and regulates tau phosphorylation and
159 (22,23). Increased *XIST* levels have been previously reported in the brains of female AD patients and
160 linked to X Chromosome Interaction, a process contributing to female-specific vulnerability in AD(24,25)

161 Notably, we observed consistent downregulation of *LY86-AS1* and *MIR7-3HG,* along with upregulation
162 of *OIP5-AS1* in AD across all cortical layers in our ST data (Fig. 5C-E). The functional roles of *LY86-*
163 *AS1* and *MIR7-3HG* are emerging, with a growing number of studies implicating these lncRNAs in
164 diverse disease contexts. *LY86-AS1* has been linked to type 2 diabetes (26), autoimmune diseases
165 (27), and the progression of multiple myeloma(28)*,* and in AD it shows a negative correlation with Braak
166 stage *(19); MIR7-3HG* has been associated with autophagy regulation and cell proliferation in cancer
167 (29), and in AD it has been related to ferroptosis and immune cell infiltration in postmortem brains(30).
168 By contrast, *OIP5-AS1* has been implicated in a broad range of diseases (31), especially cancer (32–
169 36), where it regulates key cellular processes such as proliferation, cell cycle progression, and
170 apoptosis, and modulation of inflammatory responses. In the nervous system, ischemic injury models
171 show that *OIP5-AS1* modulates neuronal apoptosis and microglia/macrophage inflammatory programs,
172 and is enriched in M2 microglia–derived exosomes (37–39). Recent integrated human data have also
173 identified the *OIP5-AS1/miR-129-5p/CREBBP* axis as a potential therapeutic target for metal toxicity–
174 induced AD pathogenesis (40).

175 Assessing cell-type expression of *OIP5-AS1* with the snRNA-seq data, we detected *OIP5-AS1* across
176 all major cell types with relatively higher expression in microglia and neurons (Fig. 5F). Orthogonal
177 validation by RNAscope combined with IHC confirmed *OIP5-AS1* signals in IBA1^{+} microglia and MAP2^{+}
178 neurons of ROSMAP DLPFC tissue sections (Fig. 5G).

179 ***OIP5-AS1* knockdown in iTF-microglia alters gene expression consistent with inflammatory**
180 **activation**

181 Motivated by above findings, we conducted functional interrogation of *OIP5-AS1* in human iPSC-
182 derived microglia. Using a line with inducible expression of six transcription factors, we generated
183 induced-transcription factor microglia-like cells (iTF-Microglia) via an eight-day protocol (Fig. 6A) (41).
184 On day 8, we transfected cells with two locked nucleic acid (LNA)-modified antisense oligonucleotides
185 (ASOs) targeting *OIP5-AS1* or a non-targeting control and then harvested cells 24 hours later for RNA-
186 seq. *OIP5-AS1* knockdown produced no detectable changes in cell viability or morphology (Fig. 6B).
187 The iTF-microglia expressed the canonical microglial marker IBA1, and the percentage of IBA1-positive
188 cells was similar between unstimulated and ASO-treated conditions (Fig. 6C), indicating that ASO
189 treatment did not impair general microglia identity.

190 Reassuringly, *OIP5-AS1* was effectively downregulated following knockdown with either ASO1 or
191 ASO2 (Fig. 6D-E; RNA-seq beta = -4.09, p = 1.69e-10). Transcriptomic profiling of *OIP5-AS1*
192 knockdown (*OIP5-AS1*-KD) cells revealed marked gene expression changes, with upregulation of
193 pathways related to innate immune signaling (*NLRP3*, *TREM1*, *CXCR2*), inflammation (*IL6*, *S100A8*,
194 *ADAM8*), cytokine response (*IRAK1*, *CHI3L1*, *TRIM27*), and rRNA processing (*NOP10*, *MRM1*,
195 *RBM28*) (Fig. 6F; Table S8). Conversely, gene sets involved in mitotic control (*BIRC5*, *PLK1*, *KIF2C*),
196 DNA methylation (*DNMT1*, *H4C14*, *H3C4*, and other histone genes), and DNA repair (*MLH1*, *BRIP1*,
197 *RPA1*) were downregulated, accompanied by a strong repression of canonical histone genes (50 of the
198 69) (Fig. S2A). These findings align with previously reported functional roles of *OIP5-AS1* in cell cycle
199 regulation and inflammation in cancer and other diseases (31,42,43). Additionally, *OIP5-AS1*
200 knockdown also resulted in downregulation of multiple genes involved in amyloid fiber formation,
201 including *APP*, *ADAM10*, and *SORL1* (Fig. 6F; Table S8), indicating a potential role of *OIP5-AS1* in
202 amyloidogenesis.

203 ***OIP5-AS1* knockdown in iTF-microglia alters cytokine secretion**

204 To evaluate the impact of *OIP5-AS*1 knockdown on immune signaling at the protein level, we performed
205 a Meso Scale multiplex immunoassay ('V-PLEX") on culture supernatants to quantify soluble cytokines
206 and chemokines 24 hours after transfection. Although variability between biological replicates was high
207 and many analytes were near the limit of detection, a few showed reproducible changes across
208 experiments. In particular, IL-6, IL-1β, IL-8 (*CXCL8*) and CCL3, all pro-inflammatory
209 cytokines/chemokines, were elevated in *OIP5-AS1*-KD cells compared to controls (Fig. 6G). Several
210 additional factors—including sICAM-1, VEGFR-1 (*FLT1*), and IL-1α—showed trends toward increased
211 secretion, though differences did not reach statistical significance (Fig. 6G). To assess potential
212 impairments in phagocytosis, we incubated control and *OIP5-AS1*-KD cells with pHrodo-labelled
213 amyloid-beta (Aβ1-42) for two hours, then assessed Aβ uptake by flow cytometry. No differences were
214 observed, with all groups phagocytosing ~90-96% of Aβ (Fig. S2B).

215 ***OIP5-AS1*-KD genes are associated with AD microglia gene signatures**

216 To evaluate whether the *OIP5-AS1*-KD transcriptional signature reflects AD-related microglia
217 programs, we performed GSEA using a set of microglia-specific AD DE genes (15). This analysis
218 revealed a negative enrichment (p=0.003), indicating that microglia AD genes were on average
219 downregulated upon *OIP5-AS1* knockdown (Fig. 6H). We next compared the *OIP5-AS1*-KD signature
220 to reported human AD microglia states (44) (Fig. 6I). We found positive enrichment for MG3 (ribosome
221 biogenesis; disease-associated microglia) and MG10 (a pro-inflammatory state), and negative
222 enrichment for MG0 (homeostatic) and MG12 (cycling) (Fig. 6I). These findings suggest that *OIP5-AS1*
223 knockdown shifts microglia gene programs toward inflammatory and disease-associated states while
224 reducing homeostatic and cycling programs.

225 **Discussion**

226 Recent advancements in sequencing technologies have revealed that a large portion of the mammalian
227 genome is transcribed into lncRNAs (1). Leveraging published ST (14) and snRNA-seq datasets (15),
228 we mapped the spatial and cellular expression of lncRNAs in DLPFC of aged human brains. We found
229 that lncRNAs exhibit greater subregion-specific expression than mRNAs and subregion-enriched
230 lncRNAs are generally not cell-type specific, and vice versa. These observations likely reflect the
231 heterogeneity of cell types within each subregion and the shared developmental origins of cell types
232 that span cortical layers. Nonetheless, the presence of subregion-specific and cell-type-specific
233 lncRNAs suggests that some lncRNAs function within precise spatial regions to support localized
234 processes, while others serve the specific needs of individual cell types.

235 For AD DE lncRNAs, we observed a moderate correlation between those identified from ST and bulk
236 RNAseq data (Fig. 3D), but only minimal overlap with results from snRNAseq (Fig. 4E). This
237 discrepancy may reflect differences in sequencing platforms as well as general technical limitations in
238 detecting lncRNAs. Whether subregion-specific or not, AD DE lncRNAs in ST data are often expressed
239 across multiple major cell types, suggesting that they may participate in multicellular and diverse
240 processes. Consistently, the lncRNA-enriched modules are enriched for diverse biological processes
241 (Fig. S1). In addition, gene set enrichment analyses (Fig. 3E) indicate the potential involvement of AD
242 DE lncRNAs in a wide range of regulatory processes, including epigenetic regulation, chromatin
243 remodeling, RNA metabolism, apoptosis, cell motility, regulation of cell death, and synaptic
244 organization.

245 Among previously reported AD DE lncRNAs (9–12,19), *OIP5-AS1* is consistently upregulated across
246 cortical subregions in our ST data from AD brains (Fig. 5C-E). Prior animal studies in brain ischemic
247 injury have shown that *OIP5-AS1* plays a pivotal role in modulating neuronal apoptosis, pyroptosis, and
248 microglia/macrophage activation and is enriched in M2 microglia–derived exosomes (37–39). In our
249 study, antisense oligonucleotide–mediated knockdown of *OIP5-AS1* in iPSC-derived microglia induced

250 robust upregulation of immune and inflammatory pathways (e.g., innate immune signaling, cytokine
251 production, acute inflammatory response) while markedly suppressing programs essential for cell cycle
252 regulation, chromatin maintenance, DNA repair, and histone expression. This dual effect mirrors
253 diverse roles of *OIP5-AS1* in other disease contexts and, importantly, recapitulates differential gene
254 expression patterns observed in maladaptive AD microglial states. Notably, recent integrated human
255 data identify the *OIP5-AS1/miR-129-5p/CREBBP* axis as a potential therapeutic target in metal toxicity–
256 induced AD pathogenesis (40). Together, these findings raise the possibility that modulating *OIP5-AS1*
257 activity could shift microglial states toward neuroprotection, providing a potential avenue for therapeutic
258 intervention in AD and related neurodegenerative diseases.

259 **Conclusions**

260 While the brain expresses more tissue-specific lncRNAs than most other tissues (45,46), their spatial
261 and cellular contexts in the human brain remain poorly understood. By leveraging our previously
262 published ST data, along with bulk and snRNA-seq data from ROSMAP participants, we mapped the
263 spatial and cellular expression of lncRNAs in brain tissue and identified spatially resolved and cell-type-
264 specific differentially expressed lncRNAs in AD. Our analysis lays the groundwork for future
265 investigations using more advanced technologies to examine lncRNA expression with greater spatial
266 and cellular resolution. Our functional perturbation experiments on *OIP5-AS1* further support the idea
267 that lncRNAs can play important roles in regulating cellular functions and may contribute to disease
268 processes. Given the relatively limited attention this area has received, our results underscore the need
269 for continued research to fully explore the functional and mechanistic roles of lncRNAs in Alzheimer's
270 disease and related brain disorders.

271 **Methods**

272 **Tissue collection for Spatial Transcriptomics**

273 The human brain tissues were obtained through the ROSMAP (Religious Orders Study and Rush
274 Memory and Aging Project) cohort studies at the Rush Alzheimer's Disease Center, Rush University
275 Medical Center (RUMC), Chicago, IL (47). Both studies were approved by the Institutional Review
276 Board of RUMC. Written informed consent was obtained as was a repository consent and an
277 Anatomic Gift Act, in compliance with national ethical guidelines. We selected 13 female individuals
278 clinically diagnosed as AD and 8 controls with no cognitive impairment (NCI) based on criteria as
279 previously reported (48–50). The brain tissue of those individuals had RIN > 5 and minimal freezing
280 artifacts. Frozen brain blocks of the right-hemisphere DLPFC were cut (~ 1 cm^3), transferred on dry
281 ice, and stored at -80°C.

282 Frozen brain blocks were embedded in OCT and cryosectioned coronally to a thickness of 10 µm
283 using a Leica CM1950 cryostat set at -17°C. Sectioning was done in sets of three (middle section for
284 ST and two adjacent sections for IF), with 10-50 µm between each set. Sections were attached to
285 Visium slides and stored at -80°C in a slide mailer for up to one week before proceeding with spatial
286 transcriptomics. ST-adjacent sections were attached to pre-labeled Leica superfrost plus slides and
287 stored at -80°C in slide mailers for up to two weeks before proceeding with immunohistochemistry.

288 **Spatial Transcriptomics**

289 Spatial Transcriptomics was performed according to the Visium Spatial Gene Expression User Guide
290 (10X Genomics; CG000239). Briefly, cryosectioned tissue on Visium slides was transferred from -
291 80°C to the lab on dry ice and quickly thawed for 1 min on a heat block at 37°C, then immediately
292 transferred to methanol pre-equilibrated to -20°C and fixed at -20°C for 30 min. Sections were then
293 stained with hematoxylin and eosin, and brightfield images were acquired with a Nikon Ti2 with NIS-
294 Elements AR 5.11.01 64-bit software. After imaging, tissues were immediately permeabilized in 0.1%
295 pepsin diluted in 0.1 M HCl for 18 min at 37°C. Reverse transcription, second-strand synthesis, cDNA

296 amplification (15 cycles), and library construction were performed according to the manufacturer's
297 instructions. For the first four individuals (#2, 8, 12, and 18), protocol version 'Rev A' was followed,
298 and the sample index PCR was 12 cycles. For the remaining samples, protocol version 'Rev D' was
299 followed, and the sample index PCR was 13-14 cycles. Library concentration was quantified by Qubit
300 1x dsDNA HS using a SpectraMax M3 plate reader. Library concentration and size distribution were
301 assessed by Fragment Analyzer (Agilent). Sequencing was performed in three batches on an Illumina
302 NovaSeq, targeting a minimum of 50,000 raw reads per spot.

303 **Spatial transcriptomics sequencing data processing**

304 Sequencing data were pre-processed with the Space Ranger pipeline (10x Genomics), which
305 mapped the barcodes against the human genome (Gencode 32), generated FASTQ files, and
306 generated a count matrix for each section. The individual files were then merged into a Seurat object
307 (Seurat v4.2.0) and were processed in R. We calculated per-spot quality metrics and spots with low-
308 measured genes (< 500) were removed. The Seurat::SCTransform function was used to normalize
309 and scale the UMI counts based on regularized negative binomial regression. Principal component
310 analysis (PCA) was performed on the top 3000 variable genes. Using the top 50 PCs and accounting
311 for technical and biological covariates such as age, RIN, library batch, and donor, we integrated the
312 datasets using the Harmony package (v0.1.0). We explored various tools for data integration and
313 chose Harmony for its high performance, usability, and scalability. We only used Harmony integration
314 to identify clusters corresponding to brain regions. All downstream analyses (differential gene
315 expression, cell proportion estimates, and ligand-receptor analysis) were performed on pre-
316 integration count data. After visualizing the standard deviation attributed to each Harmony embedding
317 as an elbow plot, we decided to use the top 10 Harmony embeddings. We applied Seurat::runUMAP
318 to compute UMAP (uniform manifold approximation and projection) dimension reduction and
319 Seurat::findNeighbors and Seurat::findClusters to identify clusters based on a shared nearest

320 neighbor (SNN) clustering algorithm (Louvain clustering with resolution set to 0.3; all other
321 parameters default). This resulted in 9 clusters, which were annotated based on their canonical
322 markers and spatialLIBD (v7.5) to the closest anatomical cortical layer (L1, L2-3, L3-5, L5, L6), white
323 matter (WM), meninges, and specific cellular subpopulations, namely cells with high expression of
324 hemoglobin genes ('Blood Vessel') and SST/NPY ('Interneuron'). The Interneuron cluster had too few
325 spots for reliable pseudobulking so was not analyzed further.Seurat::FindMarkers was used to identify
326 cluster-enriched (e.g. subregion-specific) lncRNAs reported in Fig. 2C and Table S1. For Fig. 2C, a
327 log2FC cutoff of 0.1 was employed, resulting in 50 lncRNAs.

328 **Co-expression network analysis in spatial transcriptomics**

329 The modules of co-expressed genes were derived using the Speakeasy (SE) algorithm v1, Matlab
330 version (17). We created pseudo-bulk gene expression by summing the counts per donor, then
331 splitting by ST spot cluster. Lowly expressed genes (less than 1 count per million, CPM) were
332 removed, and the variancePartition R function was applied to capture the major sources of variation,
333 as previously described (14). The input for SE consisted of the residuals after normalization using
334 tmm.voom and adjustment for library batch, RIN, age, and post-mortem interval (PMI). We built the
335 modules separately for each ST spot cluster, using the results from 100 initializations of SE and
336 Spearman correlation. This resulted in 193 modules, each with at least 30 genes (L1 = 30, L2-3 = 21,
337 L3-5 = 20, L5 = 20, L6 = 20, Meninges = 33, WM = 20, and Blood Vessels = 29). The module
338 assignments are provided in Table S2.

339 **Functional Enrichment Analysis (FEA) of Modules**

340 Each module was annotated using the gprofiler software (v2_0.2.1) via the g:GOSt R function (51).
341 This tool maps genes to functional information sources and detects statistically significantly enriched
342 terms. These sources include the GO database, pathways from KEGG, Reactome, and

343 WikiPathways, miRNA targets from miRTarBase, regulatory motif matches from TRANSFAC, tissue
344 specificity from the Human Protein Atlas, protein complexes from CORUM, and human disease
345 phenotypes from the Human Phenotype Ontology. For multiple testing correction, we used the default
346 g:SCS method unless otherwise specified. The FEA results are available in Table S4.

347 **Module Preservation (MP) Analysis**

348 To assess whether the modules were preserved across distinct ST spot clusters, we used the MP
349 function from the WGCNA R package (v1.70-3) (52). Pairwise comparisons were performed for all
350 193 modules. We then estimated the mean and variance of the preservation statistic under the null
351 hypothesis that there is no relationship between module assignments in the reference and test
352 datasets. Fifteen distinct preservation statistics were calculated (e.g., module density, mean
353 expression, connectivity), each standardized by its mean and variance to define a Z statistic for each
354 preservation measure. Under these assumptions, each Z statistic follows a normal distribution if the
355 module is not preserved. To compare preservation across modules, we calculated a composite
356 preservation measure using the following equation:
357

358 $$Zsummary = \frac{Zdensity + Zconnectivity}{2}$$
359

360 Modules with Z < 2 were considered not preserved, those with Z between 2 and 10 were considered
361 preserved, and modules with Z > 10 were considered highly preserved. Zsummary stats are available
362 in Table S3.

363 **Statistical analysis to identify AD-differential genes**

364 For each brain section of a subject, we summed the UMI counts of all spots belonging to a subregion
365 to generate a pseudobulk estimate for each gene. We only kept expressed genes with counts per

366 million (CPM) > 1 in at least 80% of the brain sections, resulting in 1,578 lncRNAs and 13,808
367 mRNAs. With the pseudobulk estimates, we estimated the library sizes of the brain sections using the
368 trimmed mean of M-values (TMM) of edgeR(53) (edgeR_3.36.0) and transformed the pseudobulk
369 estimates into $\log_2$ CPM using voom-limma (limma_3.50.1). For each subregion, we excluded brain
370 sections with <50 spots. To contrast the normalized pseudobulk expression between AD and controls,
371 we applied linear mixed models (LMM), accounting for age, PMI, RIN, and batch as fixed effects and
372 modeled within-subject correlation with a random effect. We declared significance at an α of 0.05 with
373 false discovery rate (FDR) correction across all genes and all subregions.

374 For interpretation, we applied GSEA (54) with AD-differential t-values of each subregion as scores,
375 and GO terms and canonical pathways as gene sets. To characterize lncRNAs with respect to brain
376 cell types, we used the pseudobulk expression data from a published snRNAseq dataset of 424
377 ROSMAP individuals (15). For each of the major cell types, we contrasted pseudobulk expression of
378 AD subjects vs. controls using multiple regression, accounting for age, PMI, RIN, and batch. For
379 further comparison, we repeated this AD-differential expression analysis with bulk DLPFC RNA-seq
380 data from 1049 individuals (16).

381 **RNAscope and immunofluorescence co-staining of postmortem tissue**

382 Human FFPE DLPFC sections were stained with neuron (MAP2; Sigma #M2320-100UL) and microglia
383 (IBA1; Wako #019-19741) markers followed by RNAscope with Hs-OIP5-AS1-O1-C1 probe (ACD
384 #1559738-C1) using a Bond-Rx research stainer (Leica Biosystems) using an Opal 6-plex detection kit
385 (Akoya Biosciences #NEL871001KT). Briefly, sections were baked for 30 min at 60°C prior to dewaxing
386 for 30 s at 72°C. Sections were antigen retrieved using HIER with a pH 6.0 citrate buffer solution (Leica
387 Biosystems #AR9961) for 20 min at 100°C followed by 10 min peroxide block. MAP2 (1:100) was
388 incubated for 30 min followed by 10 min Opal polymer HRP Ms+Rb and 10 min Opal signal

389 development with Opal 520 diluted at 1:100. Sections were antigen retrieved for 20 min in ph 6.0 buffer
390 again and the process is repeated with IBA1 (1:500) paired with Opal 690 (1:150). The sections were
391 then stained with RNAscope probe against *OIP5-AS1* using RNAScope LS Multiplex Fluorescent
392 Reagent Kit (ACD #322800) according to the manufacturer with the following modifications. The
393 sections were antigen retrieved using HIER with a pH 6.0 buffer for 20 min at 100°C, washed, and
394 treated with ACD Protease III for 15 min at 40°C prior to probe hybridization for 2 h at 40°C. Opal 620
395 (1:500) was used for signal development. Slides were counter stained with 10X spectral DAPI for 5 min
396 before mounting. Imaging was performed using Phenocycler-Fusion 2.0 (Akoya Biosciences) at 40X.
397 Images were spectrally umixed using inForm (Akoya Biosciences) and composite TIFs exported to
398 QuPath (v0.3.2) for quantitative analysis. Cells were defined in each ROI using QuPath Cell Detection
399 tool with the following parameters, requested pixel size = 0.5μm, background radius = 8μm, median
400 filter radius =0μm, Sigma value for Gaussian filter = 1.5μm, minimum nucleus area = 10μm2 , maximum
401 nucleus area =400μm2 , and intensity threshold = 10. Cell parameters include a cell expansion of 5 μm
402 from the cell nucleus and general parameters include smoothing of the detected nucleus/cell
403 boundaries. To quantify OIP5-AS1, subcellular spot parameters were set to detection threshold = 0.08,
404 split by intensity and shape to true, expected spot size = 0.05μm2, min spot size = 0.01μm2, max spot
405 size =1μm2 and include clusters set to true. For cell type specific expression, cells were thresholded
406 on their MAP2 and IBA1 mean cell intensity by section and cells of ambiguous identity were not included
407 in the analysis.

408 **Human iPSC-derived microglia and *OIP5AS1* knockdown**

409 The iTF-iPSC line (SF2021-173 from Kampmann lab's resource website) is a generous gift from the
410 Kampmann lab (41). Microglial differentiation was performed in 6-well or 24-well plates as described
411 above with the exception that the day 8 media change was performed on day 7 of differentiation. For
412 *OIP5-AS1* knockdown, antisense LNA GapmeRs were designed using GeneGlobe and tested in

413 cultured cells for knockdown compared to negative control A oligo (Qiagen). GapmeRs were
414 resuspended in TE at 0.5 µg/µl and stored at -20ºC. On day 8 of differentiation, GapmeRs were thawed
415 and combined with FuGENE HD (Promega) in Opti-MEM at a ratio of 1µl FuGENE:1µl GapmeR:25µl
416 Opti-MEM. Solutions were vortexed briefly and allowed to settle for 10 min before transfection. Microglia
417 in each well were treated with 2µg GapmeR for 24 h. On day 9, cells were washed briefly in PBS, and
418 RNA extraction (RNeasy, Qiagen) was performed. Samples from three biological replicates were used
419 for RNA-seq or cDNA synthesis (High-Capacity cDNA Reverse Transcription Kit, ABI). Quantitative
420 PCR assays were performed with the Taqman probe (Hs03677189_g1, ThermoFisher) normalized to
421 GAPDH.

422 **Mesoscale Multiplex Immune Biomarker Assay**

423 Conditioned media from day 9 culture was collected and frozen at -20ºC. To simultaneously assess
424 multiple immune biomarkers, conditioned media was thawed on ice, processed, and analyzed using
425 the V-PLEX Human Biomarker 39-Plex Kit (Mesoscale, K15209D-1) per the manufacturer's protocol.
426 Raw data was processed using MSD Discovery Workbench (v4) software and statistical analysis was
427 performed using GraphPad Prism 10. Comparisons between groups utilized one-way ANOVA followed
428 by Tukey's *post hoc* test and corrected p-values for multiple comparisons were reported.

429 **Amyloid beta Labeling and Phagocytosis Assay**

430 Amyloid-beta (Aβ1-42) was reconstituted and aggregated according to the Fujufilm/Cellular Dynamics
431 Labeling Amyloid Beta with pHrodo Red protocol. All reagents required to reconstitute Aβ were provided
432 in the aggregation kit (rPeptide; Cat. A-1170-2). Briefly, lyophilized Aβ was reconstituted in 250 µL 10
433 mM NaOH and transferred to a 1.5 mL microcentrifuge tube. A total of 250 µL HPLC water was added,
434 followed by 56 µL 10x TBS (pH 7.4). The reconstituted Aβ was allowed to aggregate in an incubator
435 overnight under normoxic conditions. After overnight incubation, the aggregates were collected by

436 centrifugation at 16,000 x g for 1 min at room temperature. Supernatant was removed and aggregates
437 were washed with 200 µL fresh 0.1 M NaHCO3 in water. A total of 1 mg pHrodo Red, Succinimidyl
438 Ester (ThermoFisher) was reconstituted in DMSO to a final concentration of 10 mM immediately before
439 use according to the manufacturer's protocol. pHrodo Red dye was added to supernatant-free AB
440 aggregates and mixed well. The reaction was incubated in the dark at room temperature for 1 hour.
441 The reaction tube was centrifuged as described and supernatant removed. To remove excess dye, 1
442 mL of cold methanol was added to the aggregates, and the sample was vortexed on high speed for 10
443 seconds. The reaction tube was centrifuged again and the supernatant removed. Aggregates were
444 washed with 1 mL of HBSS, vortexed on high for 10 seconds, and centrifuged before removing the
445 supernatant. Aggregates were washed an additional 3 times with HBSS as described. Finally, the
446 aggregates were resuspended in 200 uL HBSS, sonicated for 10 min, and stored at -20 ^{o}C in individual
447 aliquots.
448 On day 8 of differentiation, cells in 6-well plates were treated with GapmeRs or controls as described
449 above. On day 9, 24 hrs after treatment, Aβ was added at a dilution of 1:200 to each well for 2 h during
450 which cells were returned to a 37°C incubator. During the last 15 min of Aβ incubation, cells were
451 treated with Calcein Green AM (1:1000, Invitrogen). Media from each well was removed, and cells were
452 washed once with PBS and then treated with 1 mL of TrypLE Express. Plates were returned to the
453 incubator for 7-10 min to detach adherent cells. Cells were collected into their respective round-bottom
454 tube and the wells were washed with 1 mL of warm DMEM/F12 media to collect any remaining cells.
455 Cells were then centrifuged at 300 x g for 5 min at 4°C and supernatant discarded. FACS buffer (2%
456 BSA) was prepared by diluting 30% BSA (Fisher Scientific; Cat. No. 50-203-6474) in DPBS and was
457 used to resuspend the pelleted cells. Resuspended cells were filtered through a 70 µm mesh filter
458 immediately before data was collected by flow cytometry using the Sony SH800 Cell Sorter. Analysis
459 was performed with FlowJo v10. Single cells were gated and selected for analysis based on viability,
460 size, and complexity. The experiment was repeated for a total of three biological replicates.

461 **Immunostaining of iPSC-derived microglia**

462 iPSCs were differentiated as described above in 24 well plate format and transfected on day 8 with 0.4
463 µg per well. On day 9, samples were washed in PBS and treated with 4% paraformaldehyde (PFA;
464 Electron Microscopy Sciences, 15714-S) for 15 min. Samples were then washed three times in PBS
465 and stored at 4°C. Cells were permeabilized and blocked in 5% normal donkey serum (Jackson
466 ImmunoResearch, 017-000-121) with 0.02% Triton X-100 (Fisher, BP151-100) in PBS for 1 h at room
467 temperature. Cells were then incubated with a primary antibody (anti-IBA1 1:1000) diluted in a blocking
468 buffer for 2 h at room temperature. Cells were washed three times with PBS and then incubated with
469 secondary antibodies diluted 1:1000 in a blocking buffer for 45 min at room temperature in the dark.
470 Cells were washed three times with PBS and then stained with Hoechst 33342 (1:2000 in PBS;
471 Invitrogen, H1399) for 3 min at room temperature in the dark. Cells were washed one additional time
472 with PBS and imaged using a Nikon Eclipse Ti2-E epi-fluorescent microscope. Quantification of IBA1-
473 positive cells was done in GraphPad Prism.

474 **RNA-seq of iPSC-derived microglia**

475 RNA was extracted using the RNeasy kit (Qiagen). RNA concentration was determined using Qubit
476 broad range RNA assay (Invitrogen, Q10211) according to the manufacturer's instructions. 500 ng total
477 RNA was used for RNA-Seq library generation using the Stranded Total RNA Prep with Ribo-Zero Plus
478 (Illumina, 20040529). A Zephyr G3 NGS workstation (Perkin Elmer) was utilized to generate
479 sequencing libraries. Library size and concentrations were determined using an NGS fragment assay
480 (Agilent, DNF-473) and Qubit 1X dsDNA assay (Invitrogen) respectively, according to the
481 manufacturer's instructions. Libraries were normalized for molarity and sequenced on an Illumina
482 NovaSeq 6000 platform, generating an average of 67.50 ± 7.80 million paired-end reads per sample (2
483 × 150 bp). Transcript abundance was quantified using kallisto (v0.45.0) with GENCODE v43 gene
484 annotation, producing estimated counts matrices at transcript and gene level. With the gene level count

485 matrix, we first converted it into $\log_2$(counts per million (CPM)). For each gene, we fitted a regression
486 model with expression level as outcome and the two KD conditions and two control conditions (coded
487 as four binary variables) as covariates, and contrasted the average effect of KD against control. We
488 then applied GSEA to the resulting set of t-values.

489 **Declarations**

490 **Ethics approval and consent to participate**

491 The human brain tissues were obtained through the ROSMAP (Religious Orders Study and Memory
492 and Aging Project) cohort studies at the Rush Alzheimer's Disease Center, Rush University Medical
493 Center (RUMC), Chicago, IL., in compliance with national ethical guidelines. Both studies were
494 approved by the Institutional Review Board of RUMC.

495 **Consent for publication**

496 Written informed consent was given by the donors for brain autopsy and for the use of material and
497 clinical data for research purposes, as was a repository consent and an Anatomic Gift Act.

498 **Availability of data and materials**

499 Subregion- and cell-type-enriched lncRNAs, ST gene expression modules, AD-differential genes, and
500 knockdown-dysregulated genes are provided as supplemental tables. Raw and normalized count
501 matrices of the ST data are available at Synapse under accession code syn53141470.

502 **Competing interest**

503 The authors declare that they have no competing interests

504 **Funding**

505 This study was supported by NIA grants R01AG074082 and R01AG079223 (to Y.W.), P30AG10161,
506 P30AG72975, R01AG015819, R01AG017917, and U01AG61356 (to D. A. B.).

507 **Author contributions**

508 B.N., D.R.A., K.P.L., S.T., R.A.V., T.C., and A.I. performed data analysis. D.R.A. and S.D.T.
509 conducted ST experiments and sequencing. J.X. performed ST data processing. M.F., V.M., and
510 P.L.D. provided snRNA-seq data. H.V. and N.A.K. conducted RNAScope and IHC experiments. Y.W.,
511 B.N., D.R.A., and K.P.L. wrote the manuscript. F.S., D.S., and A.K.L. performed the microglia culture
512 and knockdown experiment. D.A.B. runs the parent ROSMAP study and provides critical input. Y.W.
513 conceived and directed this study, overseeing research activities and leading manuscript preparation.
514 All authors reviewed and approved the final manuscript.

515 **Acknowledgments**

516 We are grateful to those who agreed to donate their brains for research. We thank all the employees
517 at RADC for their support and assistance. We thank Dr. Martin Kampmann at UCSF for sharing the
518 iTF-iPSC cell line.

519 **Authors' Information**

520 Further information and requests may be directed to the corresponding author Yanling Wang
521 (Yanling_Wang@rush.edu)

522 **Materials Availability**

523 This study did not generate new unique reagents.

524 **References**

525 1. Mattick JS, Amaral PP, Carninci P, Carpenter S, Chang HY, Chen LL, et al. Long non-coding
526 RNAs: definitions, functions, challenges and recommendations. Nat Rev Mol Cell Biol. 2023
527 Jun;24(6):430–47.

528 2. Statello L, Guo CJ, Chen LL, Huarte M. Gene regulation by long non-coding RNAs and its
529 biological functions. Nat Rev Mol Cell Biol. 2020 Dec 22;22(2):96–118.

530 3. Wang KC, Chang HY. Molecular mechanisms of long noncoding RNAs. Mol Cell. 2011 Sep
531 16;43(6):904–14.

532 4. Guttman M, Amit I, Garber M, French C, Lin MF, Feldser D, et al. Chromatin signature reveals
533 over a thousand highly conserved large non-coding RNAs in mammals. Nature. 2009 Mar
534 12;458(7235):223–7.

535 5. Kung JTY, Colognori D, Lee JT. Long noncoding RNAs: past, present, and future. Genetics.
536 2013 Mar;193(3):651–69.

537 6. Djebali S, Davis CA, Merkel A, Dobin A, Lassmann T, Mortazavi A, et al. Landscape of
538 transcription in human cells. Nature. 2012 Sep 6;489(7414):101–8.

539 7. Cabili MN, Trapnell C, Goff L, Koziol M, Tazon-Vega B, Regev A, et al. Integrative annotation of
540 human large intergenic noncoding RNAs reveals global properties and specific subclasses.
541 Genes Dev. 2011 Sep 15;25(18):1915–27.

542 8. Derrien T, Johnson R, Bussotti G, Tanzer A, Djebali S, Tilgner H, et al. The GENCODE v7
543 catalog of human long noncoding RNAs: analysis of their gene structure, evolution, and
544 expression. Genome Res. 2012 Sep;22(9):1775–89.

545 9. Wu X, Xia P, Yang L, Lu C, Lu Z. The roles of long non-coding RNAs in Alzheimer's disease
546 diagnosis, treatment, and their involvement in Alzheimer's disease immune responses.
547 Noncoding RNA Res. 2024 Sep;9(3):659–66.

548 10. Policarpo R, d'Ydewalle C. Missing lnc(RNAs) in Alzheimer's Disease? Genes [Internet]. 2021
549 Dec 23;13(1). Available from: http://dx.doi.org/10.3390/genes13010039

550 11. Lan Z, Chen Y, Jin J, Xu Y, Zhu X. Long non-coding RNA: Insight into mechanisms of
551 Alzheimer's disease. Front Mol Neurosci. 2021;14:821002.

552 12. Huang Z, Zhao J, Wang W, Zhou J, Zhang J. Depletion of LncRNA NEAT1 rescues
553 mitochondrial dysfunction through NEDD4L-dependent PINK1 degradation in animal models of
554 Alzheimer's disease. Front Cell Neurosci. 2020 Feb 19;14:28.

555 13. Riva P, Ratti A, Venturin M. The Long Non-Coding RNAs in Neurodegenerative Diseases: Novel
556 Mechanisms of Pathogenesis. Curr Alzheimer Res. 2016;13(11):1219–31.

557 14. Avey DR, Ng B, Vialle RA, Kearns NA, de Paiva Lopes K, Iatrou A, et al. Uncovering plaque-Glia
558 niches in human Alzheimer's Disease brains using spatial transcriptomics. Mol Neurodegener
559 Adv [Internet]. 2025 Jul 16 [cited 2025 Aug 8]; Available from:
560 https://mnadvances.biomedcentral.com/articles/10.1186/s44477-025-00002-z

561 15. Fujita M, Gao Z, Zeng L, McCabe C, White CC, Ng B, et al. Cell subtype-specific effects of

562 genetic variation in the Alzheimer's disease brain. Nat Genet. 2024 Apr;56(4):605–14.

563 16. Mostafavi S, Gaiteri C, Sullivan SE, White CC, Tasaki S, Xu J, et al. A molecular network of the
564 aging human brain provides insights into the pathology and cognitive decline of Alzheimer's
565 disease. Nat Neurosci. 2018 Jun;21(6):811–9.

566 17. Gaiteri C, Chen M, Szymanski B, Kuzmin K, Xie J, Lee C, et al. Identifying robust communities
567 and multi-community nodes by combining top-down and bottom-up approaches to clustering. Sci
568 Rep. 2015 Nov 9;5(1):1–14.

569 18. Law CW, Chen Y, Shi W, Smyth GK. voom: Precision weights unlock linear model analysis tools
570 for RNA-seq read counts. Genome Biol. 2014 Feb 3;15(2):R29.

571 19. Cao M, Li H, Zhao J, Cui J, Hu G. Identification of age- and gender-associated long noncoding
572 RNAs in the human brain with Alzheimer's disease. Neurobiol Aging. 2019 Sep;81:116–26.

573 20. Ma P, Li Y, Zhang W, Fang F, Sun J, Liu M, et al. Long non-coding RNA MALAT1 inhibits neuron
574 apoptosis and neuroinflammation while stimulates neurite outgrowth and its correlation with MiR-
575 125b mediates PTGS2, CDK5 and FOXQ1 in Alzheimer's disease. Curr Alzheimer Res.
576 2019;16(7):596–612.

577 21. Bernard D, Prasanth KV, Tripathi V, Colasse S, Nakamura T, Xuan Z, et al. A long nuclear-
578 retained non-coding RNA regulates synaptogenesis by modulating gene expression. EMBO J.
579 2010 Sep 15;29(18):3082–93.

580 22. Dong LX, Zhang YY, Bao HL, Liu Y, Zhang GW, An FM. LncRNA NEAT1 promotes Alzheimer's
581 disease by down regulating micro-27a-3p. Am J Transl Res. 2021 Aug 15;13(8):8885–96.

582 23. Ke S, Yang Z, Yang F, Wang X, Tan J, Liao B. Long noncoding RNA NEAT1 aggravates Aβ-
583 induced neuronal damage by targeting miR-107 in Alzheimer's disease. Yonsei Med J. 2019
584 Jul;60(7):640–50.

585 24. Bajic VP, Essack M, Zivkovic L, Stewart A, Zafirovic S, Bajic VB, et al. The X files: "the mystery
586 of X chromosome instability in Alzheimer's disease." Front Genet. 2019;10:1368.

587 25. Garcia AX, Xu J, Cheng F, Ruppin E, Schäffer AA. Altered gene expression in excitatory neurons
588 is associated with Alzheimer's disease and its higher incidence in women. Alzheimers Dement (N
589 Y). 2023 Jan;9(1):e12373.

590 26. Saeidi L, Ghaedi H, Sadatamini M, Vahabpour R, Rahimipour A, Shanaki M, et al. Long non-
591 coding RNA LY86-AS1 and HCG27_201 expression in type 2 diabetes mellitus. Mol Biol Rep.
592 2018 Dec;45(6):2601–8.

593 27. Salviano-Silva A, Farias TDJ, Bumiller-Bini V, Castro M de S, Lobo-Alves SC, Busch H, et al.
594 Genetic variability of immune-related lncRNAs: polymorphisms in LINC-PINT and LY86-AS1 are
595 associated with pemphigus foliaceus susceptibility. Exp Dermatol. 2021 Jun;30(6):831–40.

596 28. Bútová R, Vychytilová-Faltejsková P, Gregorová J, Radová L, Almáši M, Bezděková R, et al.
597 LncRNAs LY86-AS1 and VIM-AS1 distinguish plasma cell leukemia patients from multiple
598 myeloma patients. Biomedicines. 2021 Nov 8;9(11):1637.

599 29. Capizzi M, Strappazzon F, Cianfanelli V, Papaleo E, Cecconi F. MIR7-3HG, a MYC-dependent
600 modulator of cell proliferation, inhibits autophagy by a regulatory loop involving AMBRA1.
601 Autophagy. 2017 Mar 4;13(3):554–66.

602 30. Tan Y, Tang W, Xiao W, Huang R, Li X, Peng W, et al. lncRNA-associated ceRNA network
603 revealing the potential regulatory roles of ferroptosis and immune infiltration in Alzheimer's
604 disease. Front Aging Neurosci. 2023 Feb 16;15:1105690.

605 31. Wooten S, Smith KN. Long non-coding RNA OIP5-AS1 (Cyrano): A context-specific regulator of
606 normal and disease processes. Clin Transl Med. 2022 Jan;12(1):e706.

607 32. Kotake Y, Matsunaga N, Wakasaki T, Okada R. OIP5-AS1 promotes proliferation of non-small-
608 cell lung cancer and head and neck squamous cell carcinoma cells. Cancer Genomics
609 Proteomics. 2021 Jul;18(4):543–8.

610 33. Wu L, Liu Y, Guo C, Shao Y. LncRNA OIP5-AS1 promotes the malignancy of pancreatic ductal
611 adenocarcinoma via regulating miR-429/FOXD1/ERK pathway. Cancer Cell Int. 2020 Jul
612 9;20(1):296.

613 34. Arunkumar G, Anand S, Raksha P, Dhamodharan S, Prasanna Srinivasa Rao H, Subbiah S, et
614 al. LncRNA OIP5-AS1 is overexpressed in undifferentiated oral tumors and integrated analysis
615 identifies as a downstream effector of stemness-associated transcription factors. Sci Rep. 2018
616 May 4;8(1):7018.

617 35. Gong M, Li Y, Song E, Li M, Qiu S, Dong W, et al. OIP5 is a novel prognostic biomarker in clear
618 cell renal cell cancer correlating with immune infiltrates. Front Immunol. 2022 Feb 15;13:805552.

619 36. Mei J, Liu G, Wang W, Xiao P, Yang D, Bai H, et al. OIP5-AS1 modulates epigenetic regulator
620 HDAC7 to enhance non-small cell lung cancer metastasis via miR-140-5p. Oncol Lett. 2020
621 Oct;20(4):7.

622 37. Chen Y, Liu W, Chen M, Sun Q, Chen H, Li Y. Up-regulating lncRNA OIP5-AS1 protects neuron
623 injury against cerebral hypoxia-ischemia induced inflammation and oxidative stress in
624 microglia/macrophage through activating CTRP3 via sponging miR-186-5p. Int
625 Immunopharmacol. 2021 Mar;92(107339):107339.

626 38. Zhu X, Li S, Ding H, Li X, Li H, Sun Q. Long non-coding RNA OIP5-AS1 protects neurons from
627 ischemia-reperfusion injury and inhibits neuronal apoptosis through TAB-2. Biochem Biophys
628 Res Commun. 2025 Jan;743(151139):151139.

629 39. Li Z, Pang Y, Hou L, Xing X, Yu F, Gao M, et al. Exosomal OIP5-AS1 attenuates cerebral
630 ischemia-reperfusion injury by negatively regulating TXNIP protein stability and inhibiting
631 neuronal pyroptosis. Int Immunopharmacol. 2024 Jan 25;127:111310.

632 40. Gupta R, Kumar P. Integrative analysis of OIP5-AS1/miR-129-5p/CREBBP axis as a potential
633 therapeutic candidate in the pathogenesis of metal toxicity-induced Alzheimer's disease. Gene
634 Rep. 2022 Mar;26(101442):101442.

635 41. Dräger NM, Sattler SM, Huang CTL, Teter OM, Leng K, Hashemi SH, et al. A CRISPRi/a
636 platform in human iPSC-derived microglia uncovers regulators of disease states. Nat Neurosci.

637 2022 Sep;25(9):1149–62.

638 42. Sun Q, Luo M, Gao Z, Han X, Wu W, Zhao H. Long non-coding RNA OIP5-AS1 aggravates
639 acute lung injury by promoting inflammation and cell apoptosis via regulating the miR-26a-
640 5p/TLR4 axis. BMC Pulm Med. 2021 Jul 14;21(1):236.

641 43. Ma J, Qian H, Zou H. Suppression of lncRNA OIP5-AS1 attenuates apoptosis and inflammation,
642 and promotes proliferation by mediating miR-25-3p expression in lipopolysaccharide-induced
643 myocardial injury. Anal Cell Pathol (Amst). 2023 Mar 20;2023:3154223.

644 44. Sun N, Victor MB, Park YP, Xiong X, Scannail AN, Leary N, et al. Human microglial state
645 dynamics in Alzheimer's disease progression. Cell. 2023 Sep 28;186(20):4386–403.e29.

646 45. Jiang C, Li Y, Zhao Z, Lu J, Chen H, Ding N, et al. Identifying and functionally characterizing
647 tissue-specific and ubiquitously expressed human lncRNAs. Oncotarget. 2016 Feb 9;7(6):7120–
648 33.

649 46. de Goede OM, Nachun DC, Ferraro NM, Gloudemans MJ, Rao AS, Smail C, et al. Population-
650 scale tissue transcriptomics maps long non-coding RNAs to complex disease. Cell. 2021 May
651 13;184(10):2633–48.e19.

652 47. Bennett DA, Buchman AS, Boyle PA, Barnes LL, Wilson RS, Schneider JA. Religious Orders
653 Study and Rush Memory and Aging Project. J Alzheimers Dis. 2018;64(s1):S161–89.

654 48. Bennett DA, Wilson RS, Schneider JA, Evans DA, Beckett LA, Aggarwal NT, et al. Natural
655 history of mild cognitive impairment in older persons. Neurology. 2002 Jul 23;59(2):198–205.

656 49. Bennett DA, Schneider JA, Arvanitakis Z, Kelly JF, Aggarwal NT, Shah RC, et al.
657 Neuropathology of older persons without cognitive impairment from two community-based
658 studies. Neurology. 2006 Jun 27;66(12):1837–44.

659 50. Bennett DA, Schneider JA, Aggarwal NT, Arvanitakis Z, Shah RC, Kelly JF, et al. Decision rules
660 guiding the clinical diagnosis of Alzheimer's disease in two community-based cohort studies
661 compared to standard practice in a clinic-based cohort study. Neuroepidemiology. 2006 Oct
662 10;27(3):169–76.

663 51. Kolberg L, Raudvere U, Kuzmin I, Adler P, Vilo J, Peterson H. g:Profiler-interoperable web
664 service for functional enrichment analysis and gene identifier mapping (2023 update). Nucleic
665 Acids Res. 2023 Jul 5;51(W1):W207–12.

666 52. Langfelder P, Luo R, Oldham MC, Horvath S. Is my network module preserved and
667 reproducible? PLoS Comput Biol. 2011 Jan 20;7(1):e1001057.

668 53. Robinson MD, McCarthy DJ, Smyth GK. edgeR: a Bioconductor package for differential
669 expression analysis of digital gene expression data. Bioinformatics. 2010 Jan 1;26(1):139–40.

670 54. Subramanian A, Tamayo P, Mootha VK, Mukherjee S, Ebert BL, Gillette MA, et al. Gene set
671 enrichment analysis: A knowledge-based approach for interpreting genome-wide expression
672 profiles. Proceedings of the National Academy of Sciences. 2005;102(43):15545–50.

673 55. Li D, Zhang J, Li X, Chen Y, Yu F, Liu Q. Insights into lncRNAs in Alzheimer's disease

674 mechanisms. RNA Biol. 2021 Jul;18(7):1037–47.

675 56. Bellenguez C, Küçükali F, Jansen IE, Kleineidam L, Moreno-Grau S, Amin N, et al. New insights
676 into the genetic etiology of Alzheimer's disease and related dementias. Nat Genet. 2022 Apr
677 4;54(4):412–36.

678

679

680

681

682

683

684

685

686

687

688

689

690

691

692

693

694

695

696

697

698

699

700

Main Figures

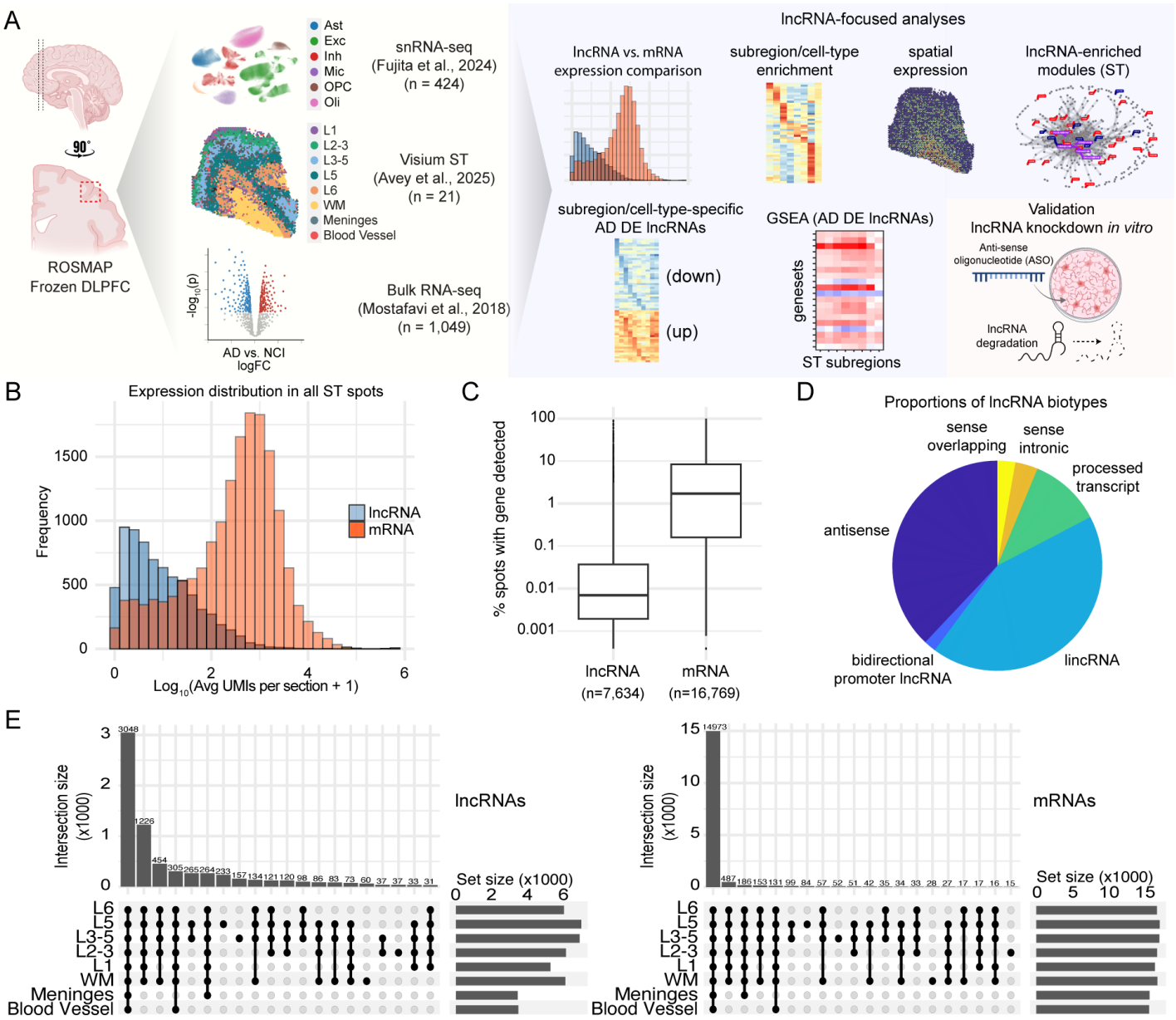

Figure 1. Spatial expression of lncRNAs. (A) Study overview. **(B)** Comparison of the expression distributions of lncRNAs and protein-coding genes (mRNAs). **(C)** Comparison of percentage of ST spots with non-zero expression for lncRNAs and mRNAs. **(D)** Proportion of detected lncRNAs (aggregated across subregions) belonging to each biotype. **(E)** Upset plots showing the numbers of lncRNAs (left) and mRNAs (right) detected in the top 20 most common intersections of subregions.

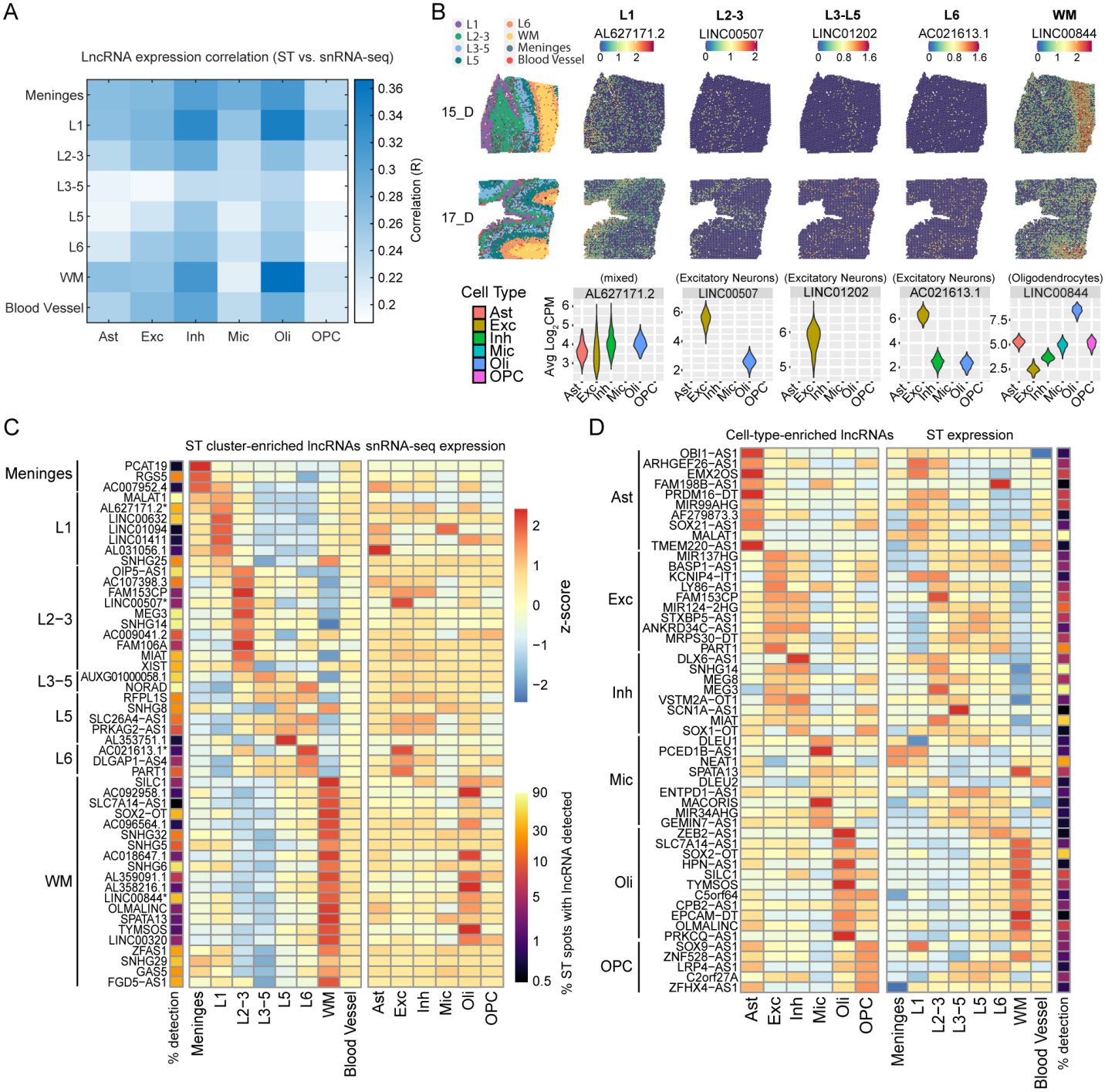

Figure 2. Enrichment of lncRNA expression by spatial subregion or cell type. (A) Correlation heatmap of ST vs. snRNA-seq expression among all co-detected lncRNAs. **(B)** UMAP and expression feature plots for two representative sections, showing 5 examples of lncRNAs with enriched expression in specific cortical layers or white matter (WM). Violin plots below show expression distributions among 6 major brain cell types. **(C)** Heatmap showing scaled expression (z-score) of the top 50 subregion-specific lncRNAs (left), and their cell-type-specific expression (right). The first column shows the percentage of spots with non-zero expression for each lncRNA. (*asterisks indicate the lncRNAs shown in panel B). **(D)** Scaled expression by cell type (left) and ST subregion (right) for the top 10 cell-type-specific lncRNAs from each of the 6 major brain cell types.

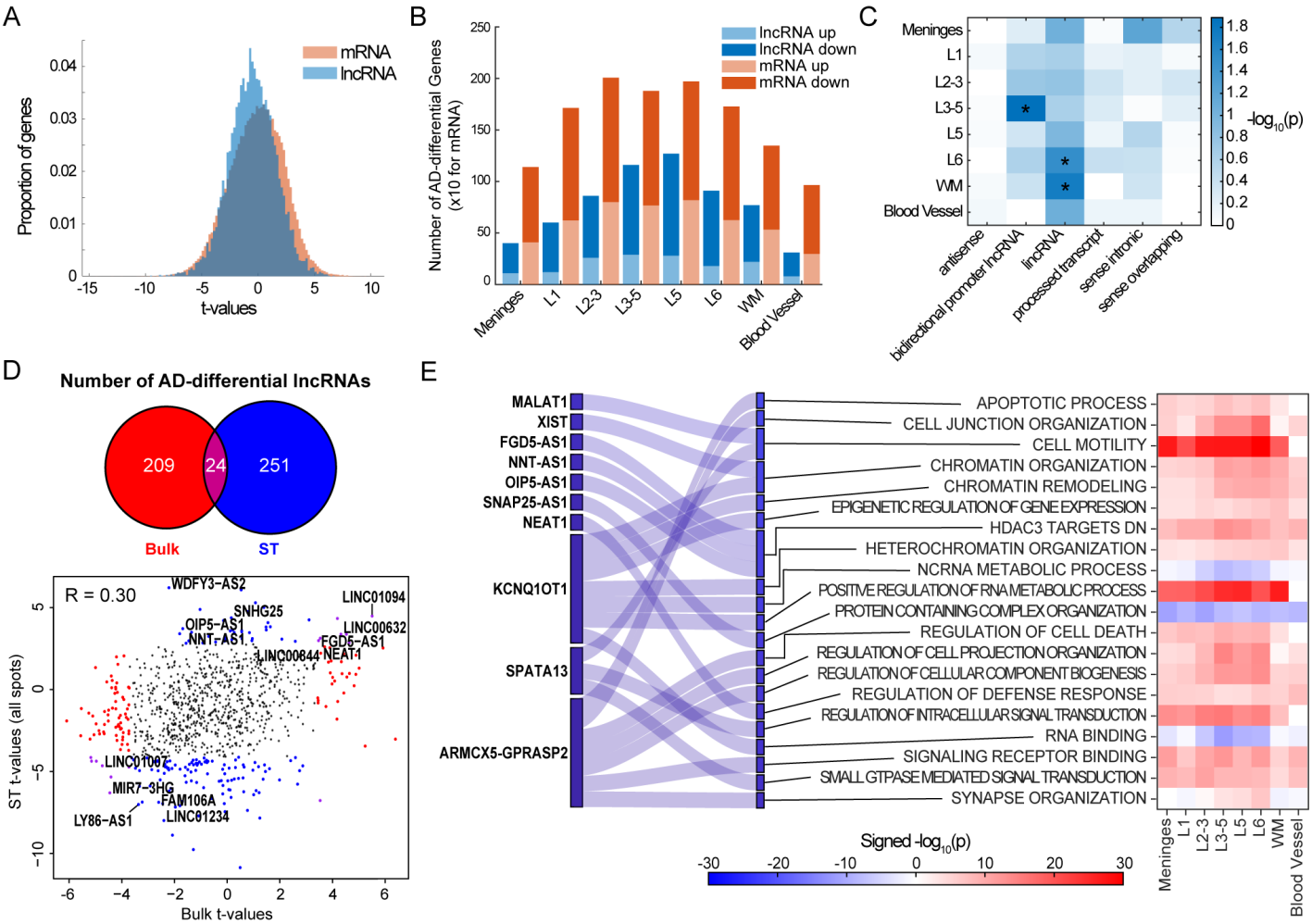

Figure 3. AD-differential lncRNAs and mRNAs identified by ST. (A) Histogram showing the distribution of AD-differential t-values for mRNAs and lncRNAs. **(B)** Total numbers of AD-differential lncRNAs and mRNAs for each subregion. **(C)** Heatmap showing the enrichment of AD-differential lncRNAs for specific biotypes (*p<0.05). **(D)** Overlaps in AD-differential lncRNAs and mRNAs between ST and bulk RNA-seq. (bottom) Scatterplot of ST (y-axis) vs. bulk RNA-seq (x-axis) of AD-differential t-values for all co-detected lncRNAs. Correlation value (R) is shown at the top left of the plot. Red dots are genes significant only based on bulk data, blue dots are genes significant based on ST data, and purple dots are genes significant for both data types. **(E)** Sankey diagram and heatmap showing a subset of enriched gene sets and AD differential lncRNAs belonging to those gene sets.

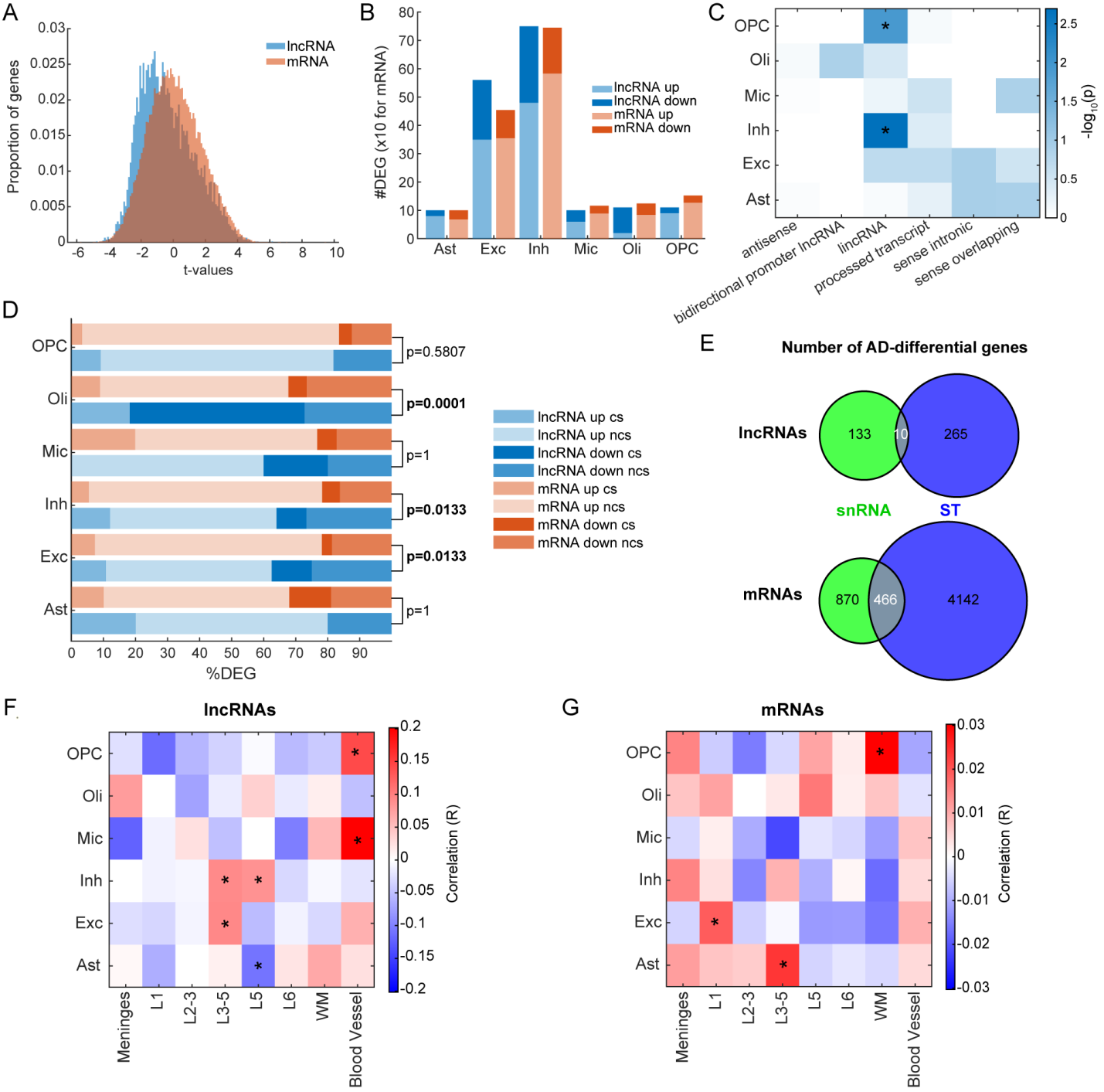

Figure 4. Cross-modality comparison of AD-differential lncRNAs. (A) Histogram showing the distribution of AD-differential t-values for mRNAs and lncRNAs based on snRNA-seq data. **(B)** Total numbers of AD-differential lncRNAs and mRNAs for each cell type. **(C)** Heatmap showing the enrichment of cell-type-specific AD-differential lncRNAs for specific biotypes. **(D)** The percentage of DEGs in each cell type, split by lncRNA/mRNA, up/down in AD, and whether they are cell-type-specific (cs) or not (ncs). Fisher's exact test was applied to assess differences in cell-type-specificity between lncRNA and mRNA with p-values indicated. **(E)** Overlaps in AD-differential lncRNAs and mRNAs between ST and snRNA-seq. **(F-G)** Heatmaps showing correlation (R) between subregions and cell types based on their AD differential t-values (*p<0.05) for lncRNAs **(F)** or mRNAs **(G)**.

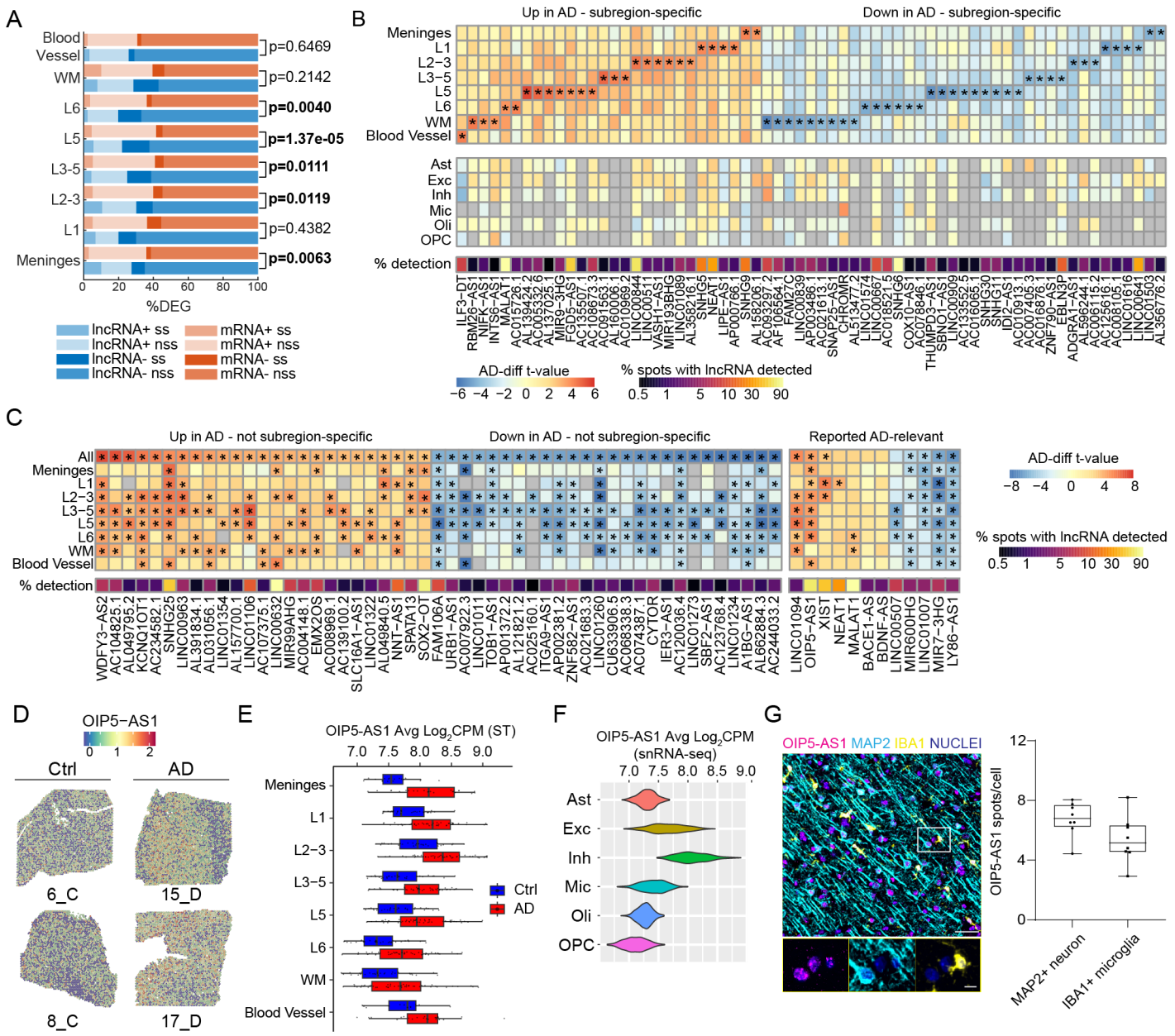

Figure 5. Subregion specificity of AD-differential lncRNAs. (A) The percentage of DEGs in each ST subregion, split by lncRNA/mRNA, up/down in AD, and whether they are subregion-specific (ss) or not (nss). Fisher's exact test was applied to assess differences in subregion-specificity between lncRNA and mRNA with p-values indicated. **(B)** (top) Heatmap showing t-values of AD-differential lncRNAs passing FDR correction specifically for one ST subregion, i.e. subregion-specific (*p<5e-4 in designated subregion and p>0.001 in all others). (bottom) AD-differential t-values for 6 brain cell types. An additional row below shows the percentage of ST spots with non-zero expression for each lncRNA. **(C)** Heatmap showing t-values of AD-differential lncRNAs passing FDR correction in two or more ST subregions, i.e. not subregion-specific (*p<5e-4). An additional row below shows the percentage of ST spots with non-zero expression for each lncRNA. **(D)** *OIP5-AS1* spatial expression plots for two control (Ctrl) and two AD sections. **(E)** Boxplot of subregion-specific pseudobulk expression of *OIP5-AS1* split by AD status. **(F)** Violin plot of cell-type-specific expression of *OIP5-AS1*. **(G)** Combined IHC/RNAScope of human postmortem DLPFC shows that *OIP5-AS1* is

762 expressed in neurons and microglia. Scale bars = 50μm upper, 10μm lower. Boxplot indicates the
763 average number of RNAscope *OIP5-AS1* spots per cell (n=8 individuals).

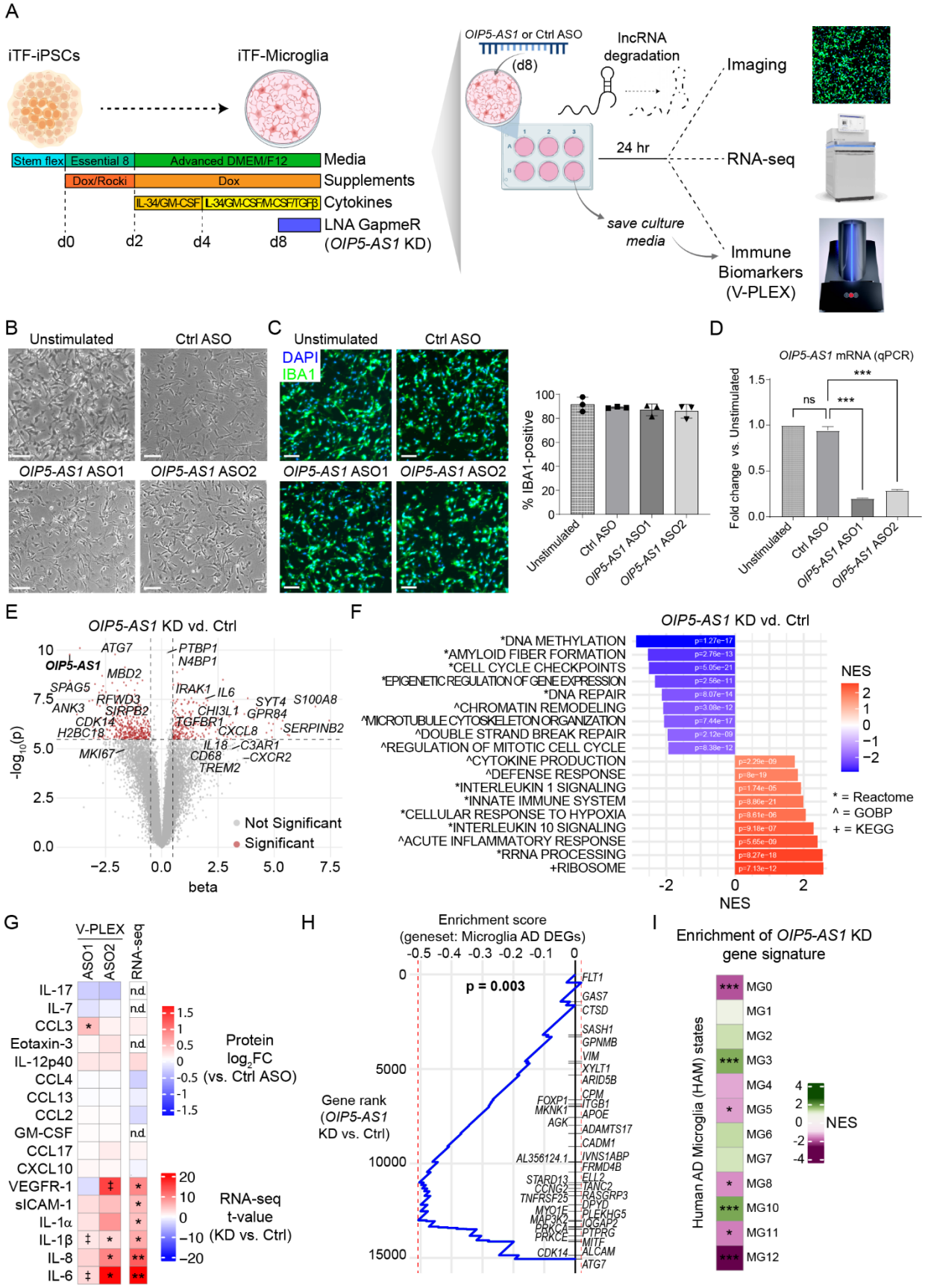
A
iTF-iPSCs
iTF-Microglia
Stem flex
Essential 8
Advanced DMEM/F12
Media
Dox/Rocki
Dox
Supplements
IL-34/GM-CSF
IL-34/GM-CSF/M-CSF/TGFβ
Cytokines
LNA GapmeR (OIP5-AS1 KD)
d0
d2
d4
d8
OIP5-AS1 or Ctrl ASO
(d8)
lncRNA degradation
Imaging
24 hr
RNA-seq
save culture media
Immune Biomarkers (V-PLEX)
B
Unstimulated
Ctrl ASO
OIP5-AS1 ASO1
OIP5-AS1 ASO2
C
Unstimulated
Ctrl ASO
DAPI
IBA1
OIP5-AS1 ASO1
OIP5-AS1 ASO2
% IBA1-positive
Unstimulated
Ctrl ASO
OIP5-AS1 ASO1
OIP5-AS1 ASO2
D
OIP5-AS1 mRNA (qPCR)
Fold change vs. Unstimulated
ns
***
Unstimulated
Ctrl ASO
OIP5-AS1 ASO1
OIP5-AS1 ASO2
E
OIP5-AS1 KD vd. Ctrl
-log10(p)
beta
OIP5-AS1
ATG7
MBD2
SPAG5
RFWD3
ANK3
SIRPB2
CDK14
H2BC18
MKI67
PTBP1
N4BP1
IRAK1
IL6
SYT4
S100A8
CHI3L1
GPR84
TGFBR1
CXCL8
SERPINB2
IL18
C3AR1
CD68
CXCR2
TREM2
Not Significant
Significant
F
OIP5-AS1 KD vd. Ctrl
*DNA METHYLATION
*AMYLOID FIBER FORMATION
*CELL CYCLE CHECKPOINTS
*EPIGENETIC REGULATION OF GENE EXPRESSION
*DNA REPAIR
^CHROMATIN REMODELING
^MICROTUBULE CYTOSKELETON ORGANIZATION
^DOUBLE STRAND BREAK REPAIR
^REGULATION OF MITOTIC CELL CYCLE
^CYTOKINE PRODUCTION
^DEFENSE RESPONSE
*INTERLEUKIN 1 SIGNALING
*INNATE IMMUNE SYSTEM
*CELLULAR RESPONSE TO HYPOXIA
*INTERLEUKIN 10 SIGNALING
^ACUTE INFLAMMATORY RESPONSE
*RRNA PROCESSING
+RIBOSOME
NES
* = Reactome
^ = GOBP
+ = KEGG
G
V-PLEX
ASO1
ASO2
RNA-seq
IL-17
IL-7
CCL3
Eotaxin-3
IL-12p40
CCL4
CCL13
CCL2
GM-CSF
CCL17
CXCL10
VEGFR-1
sICAM-1
IL-1α
IL-1β
IL-8
IL-6
n.d.
Protein log2FC (vs. Ctrl ASO)
RNA-seq t-value (KD vs. Ctrl)
H
Enrichment score (geneset: Microglia AD DEGs)
p = 0.003
Gene rank (OIP5-AS1 KD vs. Ctrl)
FLT1
GAS7
CTSD
SASH1
GPNMB
VIM
XYLT1
ARID5B
CPM
FOXP1
ITGB1
MKNK1
APOE
AGK
ADAMTS17
CADM1
AL356124.1
IVNS1ABP
FRMD4B
STARD13
ELL2
CCNG2
TANC2
TNFRSF25
RASGRP3
DPYD
MYO1E
PLEKHG5
MAP3K2
IQGAP2
PRKCA
PTPRG
PRKCE
MITF
CDK14
ALCAM
ATG7
I
Enrichment of OIP5-AS1 KD gene signature
Human AD Microglia (HAM) states
MG0
MG1
MG2
MG3
MG4
MG5
MG6
MG7
MG8
MG10
MG11
MG12
NES

Figure 6. Knockdown of *OIP5-AS1* in cultured microglia uncovers putative roles in AD-relevant biological processes. (A) Flowchart of experimental design. Inducible iPSCs were converted to microglia-like cells (iTF-Microglia) using a published protocol (ref), then transfected with ASOs targeting *OIP5-AS1* for degradation (or a non-targeting control ASO). **(B)** Phase contrast images of iTF-Microglia 24 hours post-transfection with ASOs (scale bars = 100 μm). **(C)** Immunofluorescence images of iTF-Microglia 24 hours post-transfection with ASOs (scale bars = 100 μm). Quantification is shown on the right, indicating no significant difference in the percentage of IBA1-positive cells (n=3 biological replicates). **(D)** Quantification of *OIP5-AS1* expression assessed by qPCR (***p<0.001; ns: not significant). **(E)** Volcano plot of RNA-seq results, showing beta and -$\log_{10}$(p) for all genes. Points labeled red have an abs|beta| of > 0.5 and a p<2.2e-06 (Bonferroni FDR). A subset of relevant genes are labelled. **(F)** Barplot showing NES values from GSEA of *OIP5-AS1*-KD RNA-seq for a subset of terms. **(G)** V-PLEX immunoassay results for all analytes detected above the limit of detection, for each *OIP5-AS1* ASO (*p<0.05, ⅋p<0.2). On the right is the RNA-seq t-value (KD vs. Ctrl) for the corresponding gene (n.d.: not detected; *p<2e-4, **p<2e-6). **(H)** functional GSEA of *OIP5-AS1* KD signature compared with microglia-specific AD-differential genes. AD-differential genes that reach dependent FDR (p<3.26e-05) are labelled. **(I)** GSEA NES heatmap showing enrichment of KD signature for human AD microglia (HAM) states.

Supplementary Figures

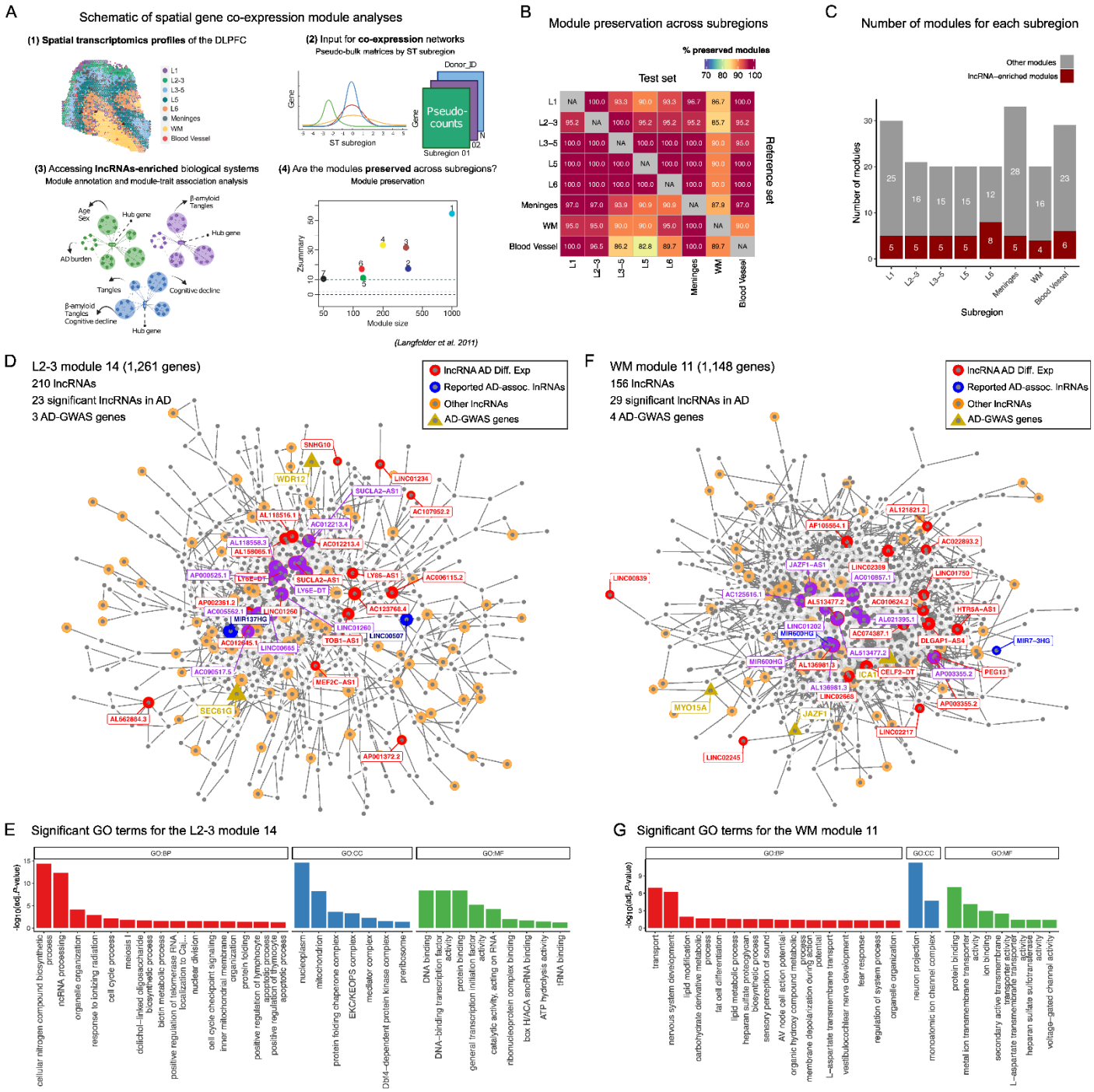

Figure S1. Subregion-specific gene modules. (A) Schematic of gene expression module generation and downstream analyses. **(B)** Heatmap showing the percentage of preserved modules between each pair of subregions. Cortical layer modules were more preserved than those derived from WM, blood vessels, and meninges. **(C)** Stacked barplot shows the number of modules in each subregion. Red colors for the lncRNA-enriched modules. Within individual subregions, 15–60% of the modules were lncRNA-enriched. **(D)** Network connectivity map for L2-3 m14, illustrating high connectivity of lncRNAs

807 (correlation > 0.9). This module was enriched with 210 lncRNAs (Bonferroni $p < 0.05$), including 4
808 reported AD-differential lncRNAs(9,10,55), 3 AD-GWAS genes(56), and 23 AD-differential lncRNA
809 genes based on our ST analysis (Tables S2, S6). **(E)** Enriched Gene Ontology (GO) terms (FDR at
810 0.05) from functional enrichment analysis of an example lncRNA-enriched module (L2-3 m14). **(F)**
811 Network connectivity map for WM module 11, illustrating high connectivity of lncRNAs (correlation >
812 0.95). This module was enriched with 156 lncRNAs (Bonferroni $p < 0.05$), including 2 previously
813 reported AD-differential lncRNAs(9,10,55), 4 AD-GWAS genes(56), and 29 AD-differential lncRNAs
814 based on our ST analysis (Tables S2, S6). **(G)** Enriched GO terms (FDR at 0.05) from functional
815 enrichment analysis for the WM module 11. **(E, G)** The GO biological process terms were collapsed,
816 keeping only the top GO parent functions to avoid redundancy. The y-axis and bar size represent the
817 significance in $-\log_{10}$(Adj. p-Value). GO biological process (BP), cellular component (CC), and GO
818 molecular function (MF).
819
820
821
822
823
824
825
826
827
828
829

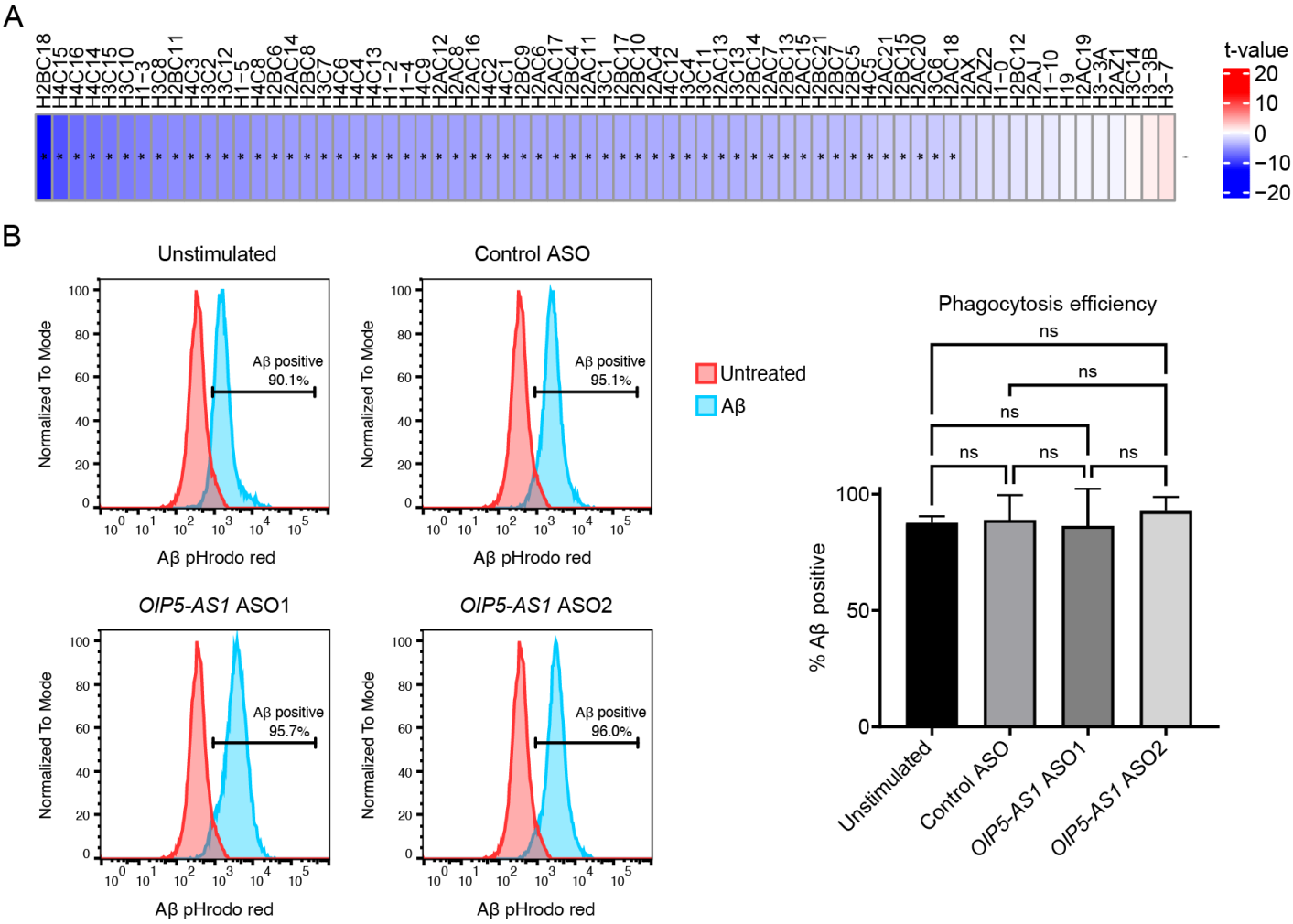

Fig. S2. *OIP5-AS1* knockdown results in widespread downregulation of histone genes and no apparent change in phagocytosis. (A) Heatmap of *OIP5-AS1*-KD vs. Ctrl t-values from RNA-seq. Fifty out of 69 detected histone genes are significantly downregulated (*p < 0.01). **(B)** Histograms of flow cytometry results following incubation of the indicated cells with pHrodo Red-labeled Aβ. The red peak indicates negative/background signal, and the blue peak indicates cells that have phagocytosed the labelled Aβ. The barplot on the right shows average percent uptake across 3 biological replicates, which was not significantly affected by *OIP5-AS1* knockdown.

845 **Supplementary Tables**

846 Table S1. Subregion- and cell-type-enriched lncRNAs

847 Table S2. ST gene expression module assignments

848 Table S3. ST gene expression module preservation

849 Table S4. ST gene expression module FEA

850 Table S5. AD-differential lncRNAs (ST, bulk, snRNA)

851 Table S6. AD-differential GSEA of ST genes

852 Table S7. AD-differential gene sets including lncRNAs

853 Table S8. DEGs and GSEA of OIP5-AS1 KD cells